Article

Revealing Ionic Signal Enhancement with Probe Grafting Density on the Outer Surface of Nanochannels

Tianle Liu, Xiaoqing Wu, Hongquan Xu, Qun Ma, Qiujiao Du, Quan Yuan, Pengcheng Gao,* and Fan Xia

Cite This: https://doi.org/10.1021/acs.analchem.1c03010

Read Online

ACCESS | Metrics & More | Article Recommendations | Supporting Information

ABSTRACT: Probe-modified nanopores/nanochannels are one of the most advanced sensors because the probes interact strongly with ions and targets in nanoconfinement and create a sensitive and selective ionic signal. Recently, ionic signals have been demonstrated to be sensitive to the probe−target interaction on the outer surface of nanopores/nanochannels, which can offer more open space for target recognition and signal conversion than nanoconfined cavities. To enhance the ionic signal, we investigated the effect of grafting density, a critical parameter of the sensing interface, of the probe on the outer surface of nanochannels on the change rate of the ionic signal before and after target recognition (β). Electroneutral peptide nucleic acids and negatively charged DNA are selected as probes and targets, respectively. The experimental results showed that when adding the same number of targets, the β value increased with the probe grafting density on the outer surface. A theoretical model with clearly defined physical properties of each probe and target has been established. Numerical simulations suggest that the decrease of the background current and the aggregation of targets at the mouth of nanochannels with increasing probe grafting density contribute to this enhancement. This work reveals the signal mechanism of probe−target recognition on the outer surface of nanochannels and suggests a general approach to the nanochannel/nanopore design leading to sensitivity improvement on the basis of relatively good selectivity.
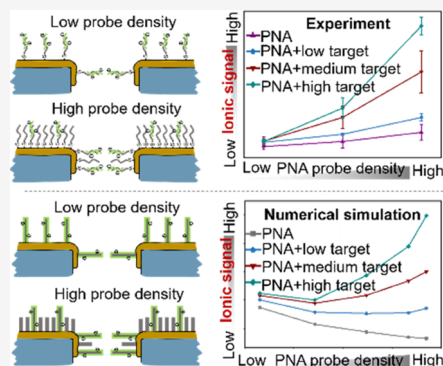
INTRODUCTION

Nanopores and nanochannels have attracted wide attention because of their pore sizes at the nanoscale level, and the corresponding spatial confinement on the ionic current inside that makes the extremely weak change of the target identifiable using ionic signals.[1−6] With the growing demands for highly sensitive sensing or even analysis at a single-molecule level, where efficient signal conversion will be needed, these systems are considered a potential solution for DNA sequencing,[7−10] trace elements analysis,[11−13] molecular chemical reaction monitoring,[14,15] and early screening of major diseases.[16−19]

The most advanced sensors, such as probe-modified solid-state nanochannels, capture targets by the probes immobilized on the surface of nanochannels, thus, further tailoring the channel−electrolyte interface and generating ionic signals.[20−23] The strong affinity between the targets and the well-chosen probes explains the high specificity of analyses.[24−31] Moreover, solid-state nanochannels are advantageous over biological nanopores in plasticity, mechanical strength, and integration.[1−3] However, because of the confined space in nanochannels, it is difficult for targets to arrive at the location of probes, thus, resulting in low recognition efficiency.[3,5,32] Nowadays, most nanopore or nanochannel research is focused on enhancing the effect of targets on the ionic current for high

sensitivity but the recognition efficiency between probes and targets has been ignored.

Recently, multiscale target recognitions from ions to cells without any limitation of the pore sizes of nanochannels have been achieved by the probe−target recognition on the outer surface of solid-state nanochannels.[33] Through the rejection by the nanochannel's mouth and the Au−thiol interaction,[34,35] in a Au-coated nanochannel with narrow pore size, the thiol-modified probes were unable to go deep into cavities and were immobilized on the outer surface and the mouth of the nanochannels. The targets captured by these probes would change the potential of the outer surface and the steric hindrance of the pore mouth, thus producing the ionic signal.[33] Compared with the narrow space inside nanochannels, the outer surface and the mouth are exposed to the solution of targets, which can not only accept probes or capture targets larger than pore sizes but also greatly improve the recognition efficiency between probes and targets.[36−40] However, until

A

now, the signaling mechanism of probe−target recognition on the outer surface of nanochannels is unclear. Meanwhile, the ionic signal needs to be further studied to trace target analysis in a complex matrix.

The aim of this work is to determine the relationship between the grafting density of probes on the outer surface and the ionic signal for sensitivity enhancement. As a significant parameter of the sensing interface, the influence of the probe grafting density in nanopores or nanochannels has been ignored for a long time because it is difficult to precisely control and characterize the distribution of probes inside the nanoconfined cavities. This effect was only roughly investigated through fluorescence characterization and numerical simulations in our previous work.[41] Now, high-resolution characterization methods, including surface charge and steric hindrance, are available for the probes on the outer surface of nanochannels.[35]

In this study, the electroneutral peptide nucleic acids (PNAs) acting as probes for DNA targets were immobilized on the outer surface of Au-deposited poly(ethylene terephthalate) (PET) nanochannels. The electrochemical method and the time-of-flight secondary ion mass spectrometry (ToF-SIMS) were used to characterize the grafting density and spatial distribution of probes and targets. The results showed that when adding the same number of targets, the change rate of the ionic signal before and after target recognition ($\beta = (I_{probe+target} - I_{probe})/I_{probe}$) under +2 V bias increased with the probe grafting density. A model of numerical simulation with independent units to describe a single PNA probe and DNA target has been established, which helped in understanding the decrease of the background current (I_{probe}) and the enhancement of target recognition at the mouth of nanochannels with the grafting density of probes. Our work reveals a combination of the precise characterization methods and the numerical simulations at a molecular level for tailoring the sensing interface and optimizing the sensing performance of nanopores or nanochannels.

■ EXPERIMENTAL METHODS

Preparation of Au-Coated Nanochannels. Nanochannel arrays with a pore diameter of 30 nm and a depth of 12 μm were prepared through chemical etching of the commercial ion-tracked poly(ethylene terephthalate) (PET) membrane.[32] A Cr layer (20 nm) and a Au layer (30 nm) were sequentially deposited on one side of the nanochannel arrays.

PNA Immobilization and DNA Hybridization. 5′-Thiolated PNA solution (30 μM) and 30 mM tris(2-carboxyethyl) phosphine hydrochloride (TCEP) were added into the Tris buffer (pH 7.4, containing Tris(hydroxymethyl) aminomethane 20 mM, NaCl 150 mM, MgCl$_2$ 5 mM) at a volume ratio of 1:10 to prepare PNA solution at different concentrations (1, 10, and 100 nM). After standing for 1 h, the solution was dropped on the Au-coated nanochannel array and allowed to react for 1 h. The array was rinsed with water and dried under argon and then added with Tris buffer containing 1 μM 6-mercapto-1-hexanol (MCH) for 1 h for surface sealing. After rinsing with water and drying under argon, the Tris buffer of DNA targets was added on the 6 mm × 6 mm PNA-modified PET membrane overnight. The volume of the solution dropped on each membrane in the above steps was 30 μL.

Characterization of the Probe Grafting Density on Nanochannels. The Au-coated PET array modified with

different grafting densities of DNA-SH, using different concentrations (1, 10, and 100 nM), was immersed in a 60 mL phosphate buffer (pH 7.4) for 15 min under a N$_2$ atmosphere. Chronocoulometry (CC) was performed from 0.2 to −0.5 V using a Pt electrode as an auxiliary electrode, a Ag/AgCl electrode as a reference electrode, and a Au-coated PET as a working electrode.[34] The electrolyte was removed after recording the forward intercept Q_0. The electrodes were operated in 0.5 mM [Ru(NH$_3$)$_6$]Cl$_3$ of PB buffer (pH 7.4) after the injection of nitrogen for 15 min to obtain the forward intercept Q_{pro}. The grafting density of thiol-modified DNA on the surface of the PET membrane was calculated using the following two equations

$$Q = \frac{2n_0 F A D_0^{0.5} c_b}{\pi^{0.5}} t^{0.5} + Q_0 + n_0 F A \lambda \tag{1}$$

$$\Gamma_{pro} = \frac{z_0 N_A}{n} \lambda \tag{2}$$

In eq 1, n_0 is the number of electrons for one [Ru(NH$_3$)$_6$]$^{3+}$ reduction, F is Faraday's constant, A is the area of the working electrode (cm^2), D_0 is the diffusion coefficient (cm^2·s^{-1}), c_b is the solution concentration (mol·cm^{-3}), and λ is the moles of [Ru(NH$_3$)$_6$]$^{3+}$ adsorption per unit area (mol·cm^{-2}). The intercept at $t = 0$ is $Q_{pro} = Q_0 + n_0 F A \lambda$ after adding [Ru(NH$_3$)$_6$]Cl$_3$. λ was calculated from $Q_{pro} - Q_0$. For eq (2), z_0 is the valence of [Ru(NH$_3$)$_6$]$^{3+}$, n is the number of DNA-SH bases, and N_A is Avogadro's constant. The probe grafting density Γ_{pro} (cm^{-2}) was obtained by substituting λ into eq 2. The sequence of thiol-modified DNA was identical to the PNA probe.

ζ Potential Measurement. A measure of 2 μL of thiol-modified PNA (30 μM) and 20 μL of TCEP (30 mM) was added into water to prepare a total volume solution of 100 μL, and then allowed to react for 1 h. After centrifugation, 100 μL of the supernatant was extracted from 600 μL of Au nanoparticle sol (1 nM), and then 100 μL of the well-reacted PNA solution was added. The sol was shaken overnight at 500 rpm in the dark at 4°. Finally, MCH was added to the sol to obtain a concentration of 1 μM. ζ Potential was measured with a Zetasizer (Nano-ZS90, Malvern Panalytical) after 1 h reaction. The DNA-SH-modified Au nanoparticle sol was prepared in the same way as described above. In addition, the ζ potentials of the untreated and directly MCH-sealed Au sol were also measured.

Ion Current Measurement. The PET membrane was clamped in the middle of a custom-made two-chamber electrochemical cell (Figure S10), and then, the cell was injected with 100 mM KCl solution. A pair of homemade Ag/AgCl electrodes were applied at both ends to apply a scanning voltage as the driving force for ion transport. An electrochemical workstation (CHI, Shanghai) was used to record $I-V$ curves.

ToF-SIMS Measurement. ToF-SIMS V (IONTOF, GmbH) was used to characterize the distribution of Au, PNA, and DNA on the surface of PET nanochannels. The depth corresponding to the PET (marked by C$_6^-$)-normalized intensity reaching 5% was considered as the position of the contact interface between Au and the nanochannel.

Numerical Simulation. The theoretical model of PNA probe modification on the outer surface of nanochannels was established using the multi-physical field software COMSOL, as shown in Figure S11. In our model, PNA molecules were
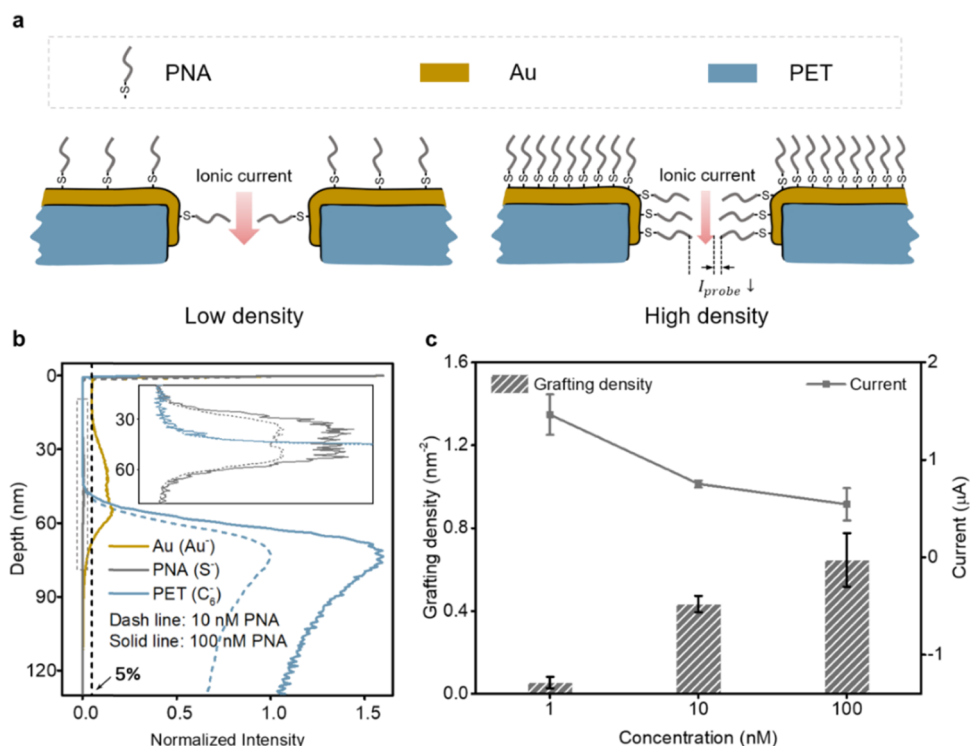
Figure 1. Experimental results of the effect of the grafting density of PNA probes on the ion current before targets were captured. (a) Schematic diagram representing the different effects of the probes with low or high grafting density on ionic currents. (b) Distribution of PNA, Au, and PET in the nanochannels characterized by ToF-SIMS. (c) Changes of the PNA probe grafting density and ion current under +2 V bias with the PNA concentration in a buffer.

uniformly distributed on the left outer surface of the nanochannel and the part with a reduced pore size (pore mouth) was in the form of a cylinder with 2 nm in length and 1 nm in diameter. The amount of PNA is proportional to the probe grafting density.

Before target hybridization, the surface charge density of the columns is zero because the PNA has no charge. When the target DNA binds to the PNA probe, the length of the column increases to 4 nm since the chain length becomes longer as the molecular chain becomes more rigid. Meanwhile, the introduction of DNA makes the probe negatively charged and its surface charge density σ_1 can be obtained by the following equation

$$\sigma_1 = \frac{q}{S} = -\frac{(n^* + 1)e}{S} \tag{3}$$

where q is the amount of charge carried by a target DNA molecule, S is the surface area of the column in contact with the solution after hybridization, n^* is the number of DNA bases, e is the elementary charge, and σ_1 is the surface charge density of PET nanopores.

The transport of cations and anions driven by the electric field can be described by the coupled Poisson–Nernst–Planck equations

$$J_i = -D_i\left(\nabla c_i + \frac{z_i c_i F}{RT}\nabla\varphi\right) + c_i u \tag{4}$$

$$\nabla^2\varphi = -\frac{F}{\varepsilon}\sum z_i c_i \tag{5}$$

$$\nabla \cdot J_i = 0 \tag{6}$$

The Nernst–Planck equation (4) describes the transport characteristics of ions in nanochannels, including diffusion, electromigration, and convection, where J_i, D_i, c_i, and z_i represent the ion flux, diffusion coefficient, concentration, and valence of each ion, respectively; φ and u represent the potential and the fluid velocity; and F, R, and T are Faraday's constant, ideal gas constant, and absolute temperature. The fluid velocity u within the nanochannels should not be neglected when the electro-osmosis effect is considered, and the flow distribution can be determined by the Navier–Stokes equation[42]

$$u\nabla u = \frac{1}{\rho}\left(-\nabla p + \eta\nabla^2 u - F\left(\sum_i z_i c_i\right)\nabla\varphi\right) \tag{7}$$

where ρ and η are the density and viscosity of the fluid, respectively, and p is the pressure; $\rho = 1 \times 10^3$ kg·m^{-3} and $\eta = 1 \times 10^{-3}$ Pa·s. In the simulation, the electrolyte solution is assumed to be incompressible ($\nabla \cdot u = 0$). The Poisson equation (5) describes the relationship between the potential of nanochannels and ion concentration, where ε is the dielectric constant of the solution; eq 6 is the steady-state condition. The coupled equations above can be solved under appropriate boundary conditions. Finally, the transmembrane ionic current (I) is calculated by integrating the ionic flux along the corresponding cross section, that is,

$$I = F\int_S\left(\sum_{i=1}^{2} z_i J_i\right)\cdot n\mathrm{d}S \tag{8}$$

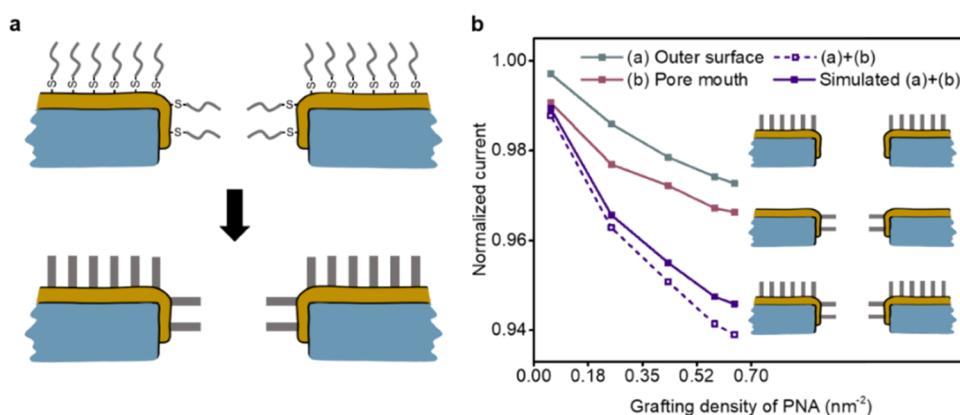where n is the normal vector of surface S.

Figure 2. Numerically simulated results of the effect of the PNA probe grafting density on the ion current before targets were captured. (a) Schematic illustration of the numerically simulated model transforming the independent probes into a unit with given physical meaning. (b) Simulated results of the effect of the grafting density of probes only on the outer surface, the pore mouth, or both the outer surface and the pore mouth.
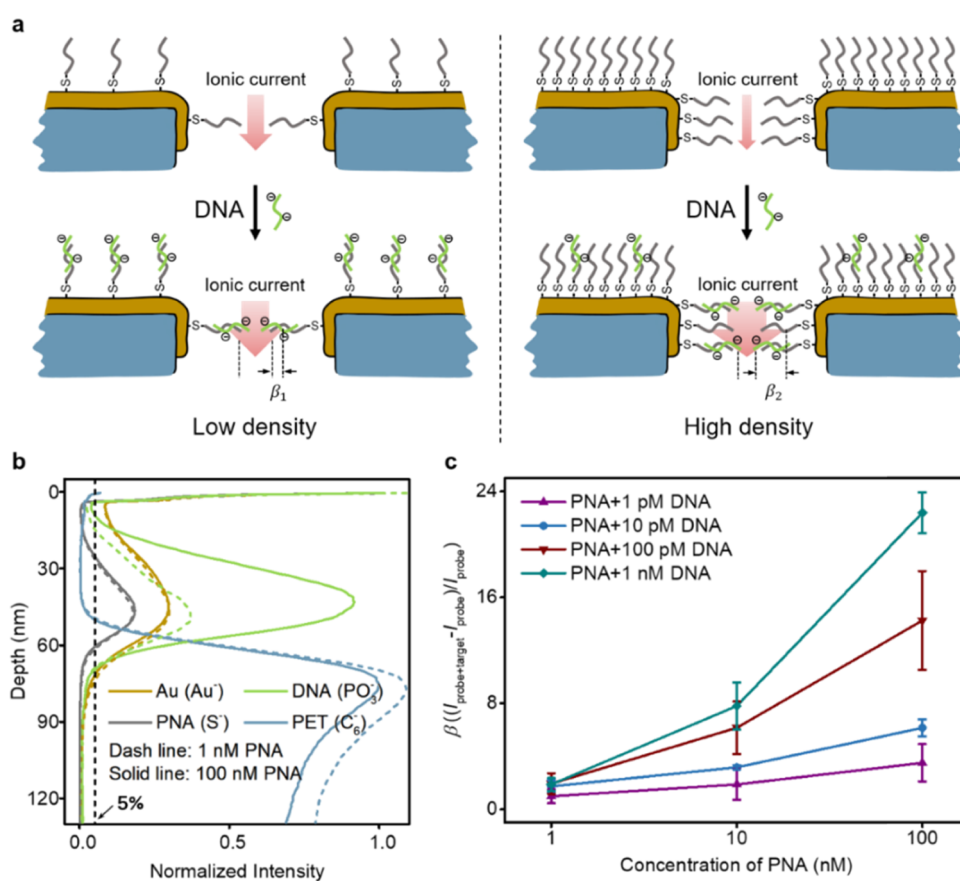

Figure 3. Experimental results of the effect of PNA probe grafting density on the ionic signal after the same amount of DNA targets were captured. (a) Schematic illustrations describe the same amount of DNA captured by the PNA of different grafting densities and its effect on the change rate of the ionic current. (b) Distribution of the PNA probes and the DNA targets in the nanochannels. Dashed and solid lines represent the element distribution in the nanochannels of low grafting density and high grafting density, respectively. (c) Relationship between the β value and the grafting density of PNA probes after hybridization with different concentrations of DNA targets.

■ RESULTS AND DISCUSSION

The Au deposition on the outer surface of the nanochannels could create a new surface, allowing thiol-modified probes to be locally immobilized on it through Au–thiol interactions.[34,35] In this work, thiol-modified PNA probes were immobilized on a Au layer with a thickness of 50 nm deposited on the outer surface of PET nanochannels (Figure 1a and

scanning electron microscopic images in Figure S1). PNA was used as a model to investigate the steric effect of the probe on the outer surface on ion transport due to its electroneutrality characteristic and hybridization with DNA via the principles of Watson–Crick base pairing.[43–46] The spatial distribution of each element in nanochannels was characterized using the ToF-SIMS, in which the signal of S^- was used to characterize the distribution of thiol-modified PNA. The ToF-SIMS results
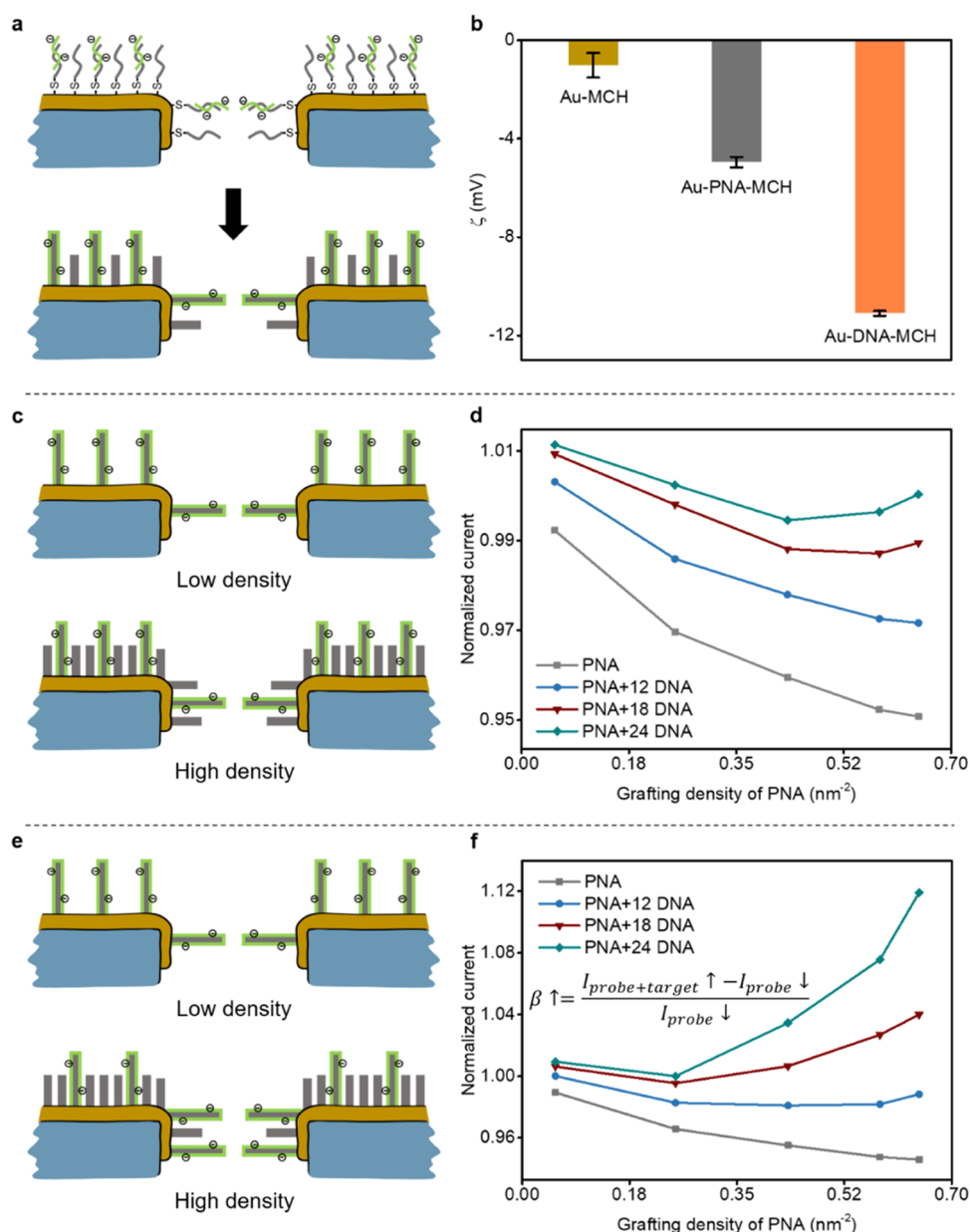
Figure 4. Establishment of the nanochannel model after the same amount of DNA targets were captured and its simulated results. (a) Schematic representation that transforms the actual situation after DNA hybridization into a physical model. (b) ζ Potential of Au nanoparticles modified with various functional molecules. (c and e) Schematic diagram of the same number of DNA targets with different distributions on the outer surface and the mouth of nanochannels. (d and f) Numerical simulation results of the relationship between the PNA probe grafting density and the ion current of the nanochannel before and after target binding.

indicated that the PNA was immobilized on the Au surface and mainly distributed on the outer surface of the nanochannels and the mouth with a depth of 15 nm (Figure 1b). When considering the intensity of Au to normalize, the intensity of the PNA at the pore mouth for the sample using higher PNA concentration in the precursor was higher, which indicates that more PNA was distributed at the pore mouth compared with the sample using a lower PNA concentration in the precursor. The grafting density of PNA probes was adjusted by adding the same volume but different concentrations of PNA within the same area of the Au layer (6 mm × 6 mm). The grafting density of DNA can be quantitatively measured by the electrochemical method of Ru(III) ions absorbed on their phosphate backbones.[33,34,47] Here, the grafting density of the PNA probes was roughly obtained by measuring the grafting density of thiol-modified DNA with the same sequence and concentration in buffer solution. With the increase of the PNA probe concentration in buffer, the grafting density of PNA increased, and the transmembrane ion current (I_{probe}) decreased, which is indicated by the current−voltage ($I-V$) curves (Figures 1c and S2).

The Poisson−Nernst−Planck (PNP) equations were used to numerically simulate the ionic current of the nanochannels with different grafting densities of PNA probes on the outer surface, in which the measured values of the grafting density and distribution of PNA were used. Commonly, the changing of the pore size reflects the change of the steric hindrance in numerical simulations.[41,48−51] However, it cannot reflect the change of the probe grafting density (Figure S3). With the construction of the geometric model for the independent
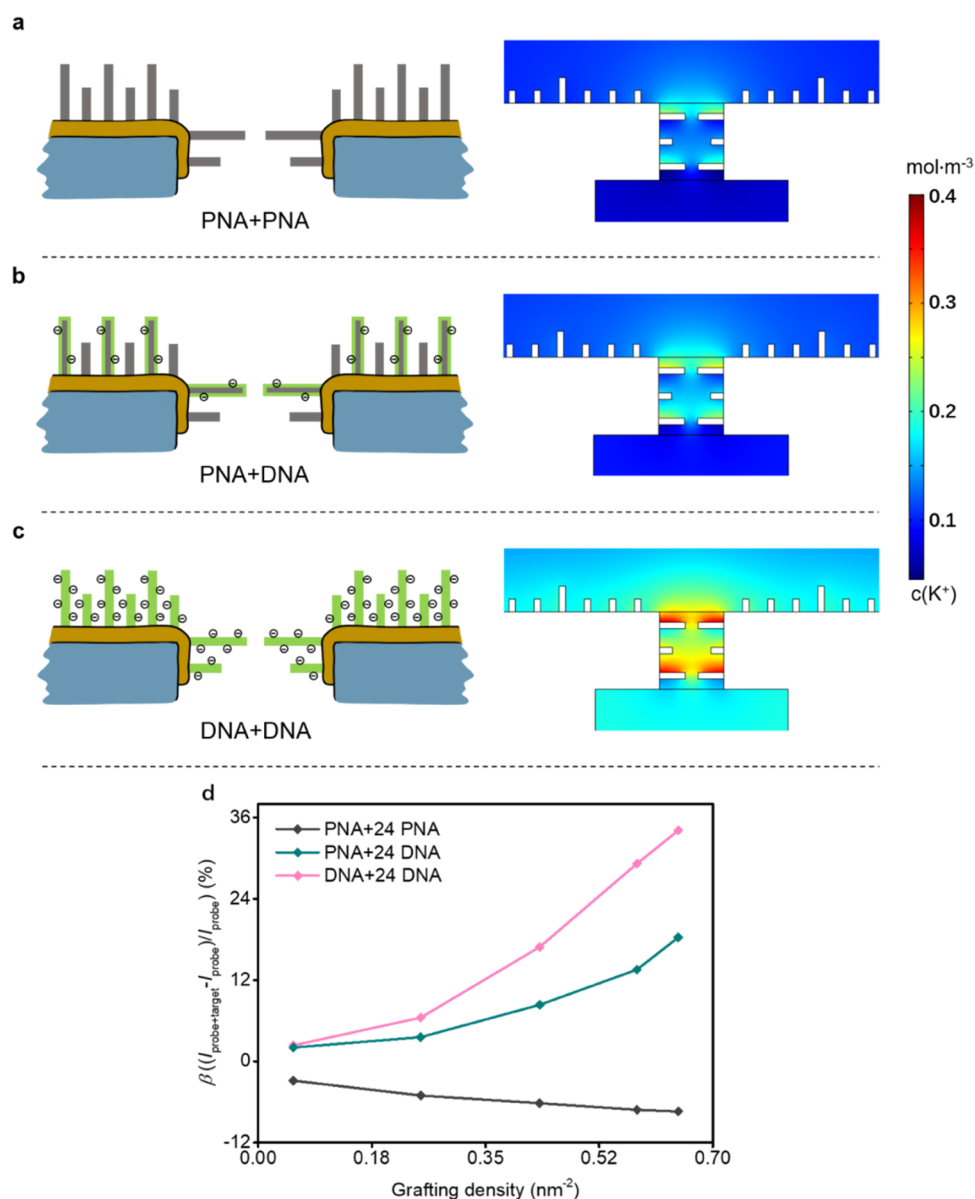
Figure 5. Simulated results of the effects of different probes and targets on β. Schematic diagram of nanochannels and cation concentration distribution after the target PNA binding to the PNA probe (a), the PNA probe capturing the target DNA (b) and the target DNA being captured by the DNA probe (c). (d) Relationship between the probe grafting density and β after the hybridization of different kinds of probes and targets with the same distribution.

probe (Figure 2a), the physical meaning of each probe has been taken into account, which precisely reflects the change of the probe grafting density. After the current I obtained by numerical simulation was normalized with the transmembrane ion current I_0 (simulated value) of Au-deposited PET without modification of any functional molecules, the normalized current results confirmed the experimental results that the steric hindrance increased with the grafting density of PNA probes, no matter whether they were immobilized at the outer surface or the pore mouth. The modification of probes on the outer surface and pore mouth caused a greater current decrease due to the combined effect of steric hindrance in the two regions. Therefore, the curve (a) + (b) in Figure 2b (calculated from $1 - (1 - \text{curve a}) - (1 - \text{curve b})$) representing the sum of the effects of steric hindrance from the two parts of probes on the current was close to the simulated result (Figure 2b

Simulated (a) + (b)) obtained when probes were immobilized at both the outer surface and pore mouth simultaneously.

We designed a series of analysis experiments using the thiol-modified PNA as the probe and its complementary DNA as the target to investigate the effect of the probe grafting density on the ionic signal. The same amount of DNA was added on the nanochannels modified with different grafting densities of PNA (Figure 3a). In the spectrum of ToF-SIMS, the distribution of DNA was characterized using PO_3^- as the marker (Figure 3b). In nanochannels with low or high probe grafting density, the distribution depth of the DNA targets was nearly the same. However, for the nanochannels with high PNA probe grafting density, the relative intensity (normalized by the intensity of Au) of the DNA target at the pore mouth was greater than that with low PNA probe grafting density. This illustrated that more DNA targets were captured at the pore mouth of the nanochannels with a higher PNA probe grafting density. This

phenomenon may be attributed to the fact that more probes were distributed at the pore mouth for the sample with a higher probe grafting density. The ionic current before (I_{probe}) and after adding the target ($I_{probe+target}$) was measured by $I-V$ tests (Figures S4 and S5). Taking the current at + 2 V for comparison, the change rate of ion current ($\beta = (I_{probe+target} - I_{probe})/I_{probe}$) was calculated. The β value reflects the conversion efficiency from target characteristics to the ionic signal, related to the sensitivity and specificity of nanopore/nanochannel analyses.[34,41,44,52−56] As shown in Figure 3c, the β increased with the grafting density of PNA, which was further confirmed by four parallel experiments using different concentrations of DNA targets.

The effect of probe grafting density on the ion current after the target being captured was investigated by numerical simulations. Based on the model shown in Figure 2, independent units were built in the simulated model to describe each charged target. Compared with a single PNA probe, the presence of hybrid complexes of the PNA probe and DNA target resulted in increases of the negative charge and vertical height, which was well reflected in the simulated model discussed above (Figure 4a). The ζ potentials of the MCH-, PNA-, and DNA-modified Au surfaces were measured and assigned to the model (Figures 4b and S6). In an ideal condition, when the distribution of the target in the nanochannel with a lower and higher probe grafting density is the same, the simulation results showed that the β value increased with the increase of the PNA grafting density (Figures 4c and S7a). It was mainly attributed to the decrease of I_{probe} (Figure 4d). In the actual situation, the higher grafting density of the probe leads to more DNA molecules at the pore mouth (Figure 3b). The results of the model consistent with the facts showed that β also increased with the probe grafting density and was greater than that in the ideal condition (Figures 4e and S7b). This phenomenon resulted from the decrease of I_{probe} as described above and the increase of $I_{probe+target}$ because of more negatively charged targets being captured at the pore mouth (Figure 4f). The simulation results of the relationship between the number of DNA targets distributed in different regions of the nanochannel and β under the same probe grafting density further illustrate the above phenomenon (Figure S8).

We further theoretically investigated the effect of the target at the mouth of the nanochannel on ionic signals.[31,57] Since the present model is able to set the steric hindrance and the charge of each probe and target, three models have been established using different types of probes and targets but with the same distribution, including model 1 of electroneutral PNA probe and PNA target, model 2 of electroneutral PNA probe and the negatively charged DNA target and model 3 of the negatively charged DNA probe and DNA target (Figure 5a−c). In model 1, the β value was negative and decreased with the grafting density of PNA probes, which resulted from the increase of steric hindrance and the decrease of $I_{probe+target}$ by adding the PNA target (Figures 5d and S9). Compared with model 2, the β value of model 3 was greater. Color maps of K$^+$ ions in the nanochannel at +2 V indicated that a great aggregation of K$^+$ ions occurred around the negatively charged PNA + DNA or DNA + DNA complexes (Figure 5a−c). Compared with PNA + DNA complexes, the double negative charge of DNA + DNA complexes enhanced the effect of the electric double layer and the corresponding ionic signal. These results indicated that both the change of probe and the distribution of the target in

the channel would change the β value, which is a critical ionic signal reflecting the sensitivity and selectivity of nanopore/nanochannel analyses.

■ CONCLUSIONS

In conclusion, we have investigated the effect of probe grafting density on the outer surface of nanochannels on the ionic current theoretically and experimentally. Electroneutral PNA and negatively charged DNA were used as probes and targets, respectively. In the experimental means, electrochemical methods using Ru(III) ions as markers and ToF-SIMS have been applied to precisely characterize the grafting density and distribution of probes. In the theoretical means, refined models in numerical simulation with the specific definition of each probe have been built, which reflect the effect of the probe grafting density on the ionic signal. The theoretical and experimental results were in good agreement with each other, confirming that the change rate of the ion current increased with the probe grafting density. More importantly, *de novo* characterization methods and simulated models have been established to precisely investigate the effect of the spatial distribution of the probe and the target on the ionic signal.

■ ASSOCIATED CONTENT

Ⓢ Supporting Information

The Supporting Information is available free of charge at https://pubs.acs.org/doi/10.1021/acs.analchem.1c03010.

> Materials; SEM images of PET porous membrane; effect of the probe grafting density on the ionic current before target binding simulated by the common model; $I-V$ curves of PET nanochannels after the modification of PNA probes with different concentrations and hybridization with target DNA; experimental results of ionic current variation with the PNA probe grafting density before adding target and after DNA hybridization; ζ potentials of untreated, directly MCH-sealed, and PNA- or DNA-modified Au nanoparticles; numerical simulation results of the relationship between the PNA probe grafting density and the change rate of the ion current; numerical simulation results of the relationship between the number of DNA targets distributed in different regions of the nanochannel and the ionic signal; effect of the probe grafting density on the ion current simulated with different probes and targets; transmembrane ion current measurement device; models and boundary conditions used in numerical simulations; and PNA and DNA sequences used in this work (PDF)

■ AUTHOR INFORMATION

Corresponding Author

Pengcheng Gao − *State Key Laboratory of Biogeology and Environmental Geology, Engineering Research Center of Nano-Geomaterials of Ministry of Education, Faculty of Materials Science and Chemistry, China University of Geosciences, Wuhan 430074, P. R. China;* ⓞ orcid.org/0000-0002-9209-5312; Email: pcgao@cug.edu.cn

Authors

Tianle Liu − *State Key Laboratory of Biogeology and Environmental Geology, Engineering Research Center of Nano-Geomaterials of Ministry of Education, Faculty of*

Materials Science and Chemistry, China University of Geosciences, Wuhan 430074, P. R. China

Xiaoqing Wu − *State Key Laboratory of Biogeology and Environmental Geology, Engineering Research Center of Nano-Geomaterials of Ministry of Education, Faculty of Materials Science and Chemistry, China University of Geosciences, Wuhan 430074, P. R. China*

Hongquan Xu − *State Key Laboratory of Biogeology and Environmental Geology, Engineering Research Center of Nano-Geomaterials of Ministry of Education, Faculty of Materials Science and Chemistry, China University of Geosciences, Wuhan 430074, P. R. China*

Qun Ma − *State Key Laboratory of Biogeology and Environmental Geology, Engineering Research Center of Nano-Geomaterials of Ministry of Education, Faculty of Materials Science and Chemistry, China University of Geosciences, Wuhan 430074, P. R. China*

Qiujiao Du − *School of Mathematics and Physics, China University of Geosciences, Wuhan 430074, P. R. China*

Quan Yuan − *Institute of Chemical Biology and Nanomedicine, State Key Laboratory of Chemo/Biosensing and Chemometrics, College of Chemistry and Chemical Engineering, Hunan University, Changsha 410000, P. R. China;* orcid.org/0000-0002-3085-431X

Fan Xia − *State Key Laboratory of Biogeology and Environmental Geology, Engineering Research Center of Nano-Geomaterials of Ministry of Education, Faculty of Materials Science and Chemistry, China University of Geosciences, Wuhan 430074, P. R. China;* orcid.org/0000-0001-7705-4638

Complete contact information is available at:
https://pubs.acs.org/10.1021/acs.analchem.1c03010

Author Contributions

The manuscript was written through contributions of all authors. All authors have given approval to the final version of the manuscript.

Notes

The authors declare no competing financial interest.

■ REFERENCES

(1) Howorka, S. *Nat. Nanotechnol.* **2017**, *12*, 619−630.
(2) Zhang, Z.; Wen, L.; Jiang, L. *Chem. Soc. Rev.* **2018**, *47*, 322−356.
(3) Bocquet, L. *Nat. Mater.* **2020**, *19*, 254−256.
(4) Ying, Y.; Long, Y. *J. Am. Chem. Soc.* **2019**, *141*, 15720−15729.
(5) Xue, L.; Yamazaki, H.; Ren, R.; Wanunu, M.; Ivanov, A. P.; Edel, J. B. *Nat. Rev. Mater.* **2020**, *5*, 931−951.
(6) Vlassiouk, I.; Kozel, T. R.; Siwy, Z. S. *J. Am. Chem. Soc.* **2009**, *131*, 8211−8220.
(7) Traversi, F.; Raillon, C.; Benameur, S. M.; Liu, K.; Khlybov, S.; Tosun, M.; Krasnozhon, D.; Kis, A.; Radenovic, A. *Nat. Nanotechnol.* **2013**, *8*, 939−945.
(8) Belkin, M.; Chao, S.; Jonsson, M. P.; Dekker, C.; Aksimentiev, A. *ACS Nano* **2015**, *9*, 10598−10611.
(9) Feng, J.; Liu, K.; Bulushev, R. D.; Khlybov, S.; Dumcenco, D.; Kis, A.; Radenovic, A. *Nat. Nanotechnol.* **2015**, *10*, 1070−1076.
(10) Zhu, Z.; Duan, X.; Li, Q.; Wu, R.; Wang, Y.; Li, B. *J. Am. Chem. Soc.* **2020**, *142*, 4481−4492.
(11) Liu, L.; Yang, C.; Zhao, K.; Li, J.; Wu, H. *Nat. Commun.* **2013**, *4*, No. 2989.
(12) Wang, C.; Zhao, X.; Liu, F.; Chen, Y.; Xia, X.; Li, J. *Nano Lett.* **2020**, *20*, 1846−1854.
(13) Cai, S.; Sze, J. Y. Y.; Ivanov, A. P.; Edel, J. B. *Nat. Commun.* **2019**, *10*, No. 1797.
(14) Ying, Y.; Li, Y.; Mei, J.; Gao, R.; Hu, Y.; Long, Y.; Tian, H. *Nat. Commun.* **2018**, *9*, No. 3657.
(15) Zhu, L.; Zhang, Z.; Liu, Q. *Anal. Chem.* **2020**, *92*, 13238−13245.
(16) Shi, L.; Mu, C.; Gao, T.; Chai, W.; Sheng, A.; Chen, T.; Yang, J.; Zhu, X.; Li, G. *J. Am. Chem. Soc.* **2019**, *141*, 8239−8243.
(17) He, X.; Zhang, K.; Liu, Y.; Wu, F.; Yu, P.; Mao, L. *Angew. Chem.* **2018**, *130*, 4680−4683.
(18) Sun, Y.; Chen, S.; Chen, X.; Xu, Y.; Zhang, S.; Ouyang, Q.; Yang, G.; Li, H. *Nat. Commun.* **2019**, *10*, No. 1323.
(19) Fan, Y.; Sheng, Z.; Chen, J.; Pan, H.; Chen, B.; Wu, F.; Wang, S.; Chen, X.; Hou, X. *Angew. Chem., Int. Ed.* **2019**, *58*, 3967−3971.
(20) Wei, R.; Gatterdam, V.; Wieneke, R.; Tampé, R.; Rant, U. *Nat. Nanotechnol.* **2012**, *7*, 257−263.
(21) Howorka, S.; Siwy, Z. *Chem. Soc. Rev.* **2009**, *38*, 2360−2384.
(22) Bocquet, L.; Charlaix, E. *Chem. Soc. Rev.* **2010**, *39*, 1073−1095.
(23) Pérez-Mitta, G.; Toimil-Molares, M. E.; Trautmann, C.; Marmisollé, W. A.; Azzaroni, O. *Adv. Mater.* **2019**, *31*, 1901483−1901529.
(24) Li, M.; Xiong, Y.; Lu, W.; Wang, X.; Liu, Y.; Na, B.; Qin, H.-J.; Tang, M.; Qin, H.-Q.; Ye, M.; Liang, X.; Qing, G. *J. Am. Chem. Soc.* **2020**, *142*, 16324−16333.
(25) Chen, H.; Xu, L.; Tuo, W.; Chen, X.; Huang, J.; Zhang, X.; Sun, Y. *Anal. Chem.* **2020**, *92*, 4131−4136.
(26) Wang, Y.; Yang, Q.; Zhao, M.; Wu, J.; Su, B. *Anal. Chem.* **2018**, *90*, 10780−10785.
(27) Ma, T.; Balanzat, E.; Janot, J. M.; Balme, S. *Biosens. Bioelectron.* **2019**, *137*, 207−212.
(28) Boussouar, I.; Chen, Q.; Chen, X.; Zhang, Y.; Zhang, F.; Tian, D.; White, H. S.; Li, H. *Anal. Chem.* **2017**, *89*, 1110−1116.
(29) Steel, A. B.; Herne, T. M.; Tarlov, M. J. *Anal. Chem.* **1998**, *70*, 4670−4677.
(30) Giamblanco, N.; Janot, J. M.; Gubbiotti, A.; Chinappi, M.; Balme, S. *Small Methods* **2020**, *4*, No. 1900703.
(31) Buchsbaum, S. F.; Nguyen, G.; Howorka, S.; Siwy, Z. S. *J. Am. Chem. Soc.* **2014**, *136*, 9902−9905.
(32) Xu, X.; Zhao, W.; Gao, P.; Li, H.; Feng, G.; Zhao, Z.; Lou, X. *NPG Asia Mater.* **2016**, *8*, No. e234.
(33) Ma, Q.; Li, Y.; Wang, R.; Xu, H.; Du, Q.; Gao, P.; Xia, F. *Nat. Commun.* **2021**, *12*, No. 1573.
(34) Li, X.; Zhai, T.; Gao, P.; Cheng, H.; Hou, R.; Lou, X.; Xia, F. *Nat. Commun.* **2018**, *9*, No. 40.
(35) Gao, P.; Ma, Q.; Ding, D.; Wang, D.; Lou, X.; Zhai, T.; Xia, F. *Nat. Commun.* **2018**, *9*, No. 4557.
(36) Tagliazucchi, M.; Rabin, Y.; Szleifer, I. *ACS Nano* **2013**, *7*, 9085−9097.
(37) Tagliazucchi, M.; Rabin, Y.; Szleifer, I. *J. Am. Chem. Soc.* **2011**, *133*, 17753−17763.
(38) Cao, L.; Wen, Q.; Feng, Y.; Ji, D.; Li, H.; Li, N.; Jiang, L.; Guo, W. *Adv. Funct. Mater.* **2018**, *28*, 1804189−1804195.
(39) Wang, C.; Fu, Q.; Wang, X.; Kong, D.; Sheng, Q.; Wang, Y.; Chen, Q.; Xue, J. *Anal. Chem.* **2015**, *87*, 8227−8233.

(40) Zhao, X.; Liu, F.; Hu, W.; Younis, M. R.; Wang, C.; Xia, X. *Anal. Chem.* **2019**, *91*, 3582−3589.

(41) Ma, Q.; Liu, T.; Xu, R.; Du, Q.; Gao, P.; Xia, F. *Anal. Chem.* **2021**, *93*, 1984−1990.

(42) White, H. S.; Bund, A. *Langmuir* **2008**, *24*, 2212−2218.

(43) Nielsen, P. E. *Curr. Opin. Biotechnol.* **1999**, *10*, 71−75.

(44) Ali, M.; Neumann, R.; Ensinger, W. *ACS Nano* **2010**, *4*, 7267−7274.

(45) Startsev, M. A.; Ostrowski, M.; Goldys, E. M.; Inglis, D. W. *Electrophoresis* **2017**, *38*, 335−341.

(46) Wu, Y.; Wang, D.; Willner, I.; Tian, Y.; Jiang, L. *Angew. Chem., Int. Ed.* **2018**, *57*, 7790−7794.

(47) Lin, M.; Song, P.; Zhou, G.; Zuo, X.; Aldalbahi, A.; Lou, X.; Shi, J.; Fan, C. *Nat. Protoc.* **2016**, *11*, 1244−1263.

(48) Cai, J.; He, Q.; Song, L.; Han, L.; Liu, B.; Zhao, Y.; Chen, W.; Zhan, D. *J. Phys. Chem. C* **2019**, *123*, 26299−26308.

(49) Hsu, J.-P.; Su, T.-C.; Peng, P.-H.; Hsu, S.-C.; Zheng, M.-J.; Yeh, L.-H. *ACS Nano* **2019**, *13*, 13374−13381.

(50) Lan, W.; Edwards, M. A.; Luo, L.; Perera, R. T.; Wu, X.; Martin, C. R.; White, H. S. *Acc. Chem. Res.* **2016**, *49*, 2605−2613.

(51) Li, H.; Xiao, F.; Hong, G.; Su, J.; Li, N.; Cao, L.; Wen, Q.; Guo, W. *Chin. J. Chem.* **2019**, *37*, 469−473.

(52) Ma, Q.; Si, Z.; Li, Y.; Wang, D.; Wu, X.; Gao, P.; Xia, F. *TrAC, Trends Anal. Chem.* **2019**, *115*, 174−186.

(53) Sun, Z.; Liao, T.; Zhang, Y.; Shu, J.; Zhang, H.; Zhang, G. *Biosens. Bioelectron.* **2016**, *86*, 194−201.

(54) Xiong, H.; Zheng, X. *Analyst* **2014**, *139*, 1732−1739.

(55) Zhao, F.; Zhang, H.; Zheng, J. *Sens. Actuators, B* **2021**, *327*, No. 128898.

(56) Xu, J.; Liao, K.; Fu, Z.; Xiong, Z. *Artif. Cells, Nanomed., Biotechnol.* **2019**, *47*, 2634−2640.

(57) Lin, C.-Y.; Combs, C.; Su, Y.-S.; Yeh, L.-H.; Siwy, Z. S. *J. Am. Chem. Soc.* **2019**, *141*, 3691−3698.